

Electronic transport evolution across the successive structural transitions in $Ni_{50-x}Fe_xTi_{50}$ shape memory alloys

Ping He(何萍), Jinying Yang(杨金颖), Qiusa Ren(任秋飒), Binbin Wang(王彬彬), Guangheng Wu(吴光恒), and Enke Liu(刘恩克)

Citation: Chin. Phys. B, 2024, 33 (**7**): 077201. DOI: 10.1088/1674-1056/ad39d3
Journal homepage: http://cpb.iphy.ac.cn; http://iopscience.iop.org/cpb

What follows is a list of articles you may be interested in

Anisotropic spin transport and photoresponse characteristics detected by tip movement in magnetic single-molecule junction

Deng-Hui Chen(陈登辉), Zhi Yang(羊志), Xin-Yu Fu(付新宇), Shen-Ao Qin(秦申奥), Yan Yan(严岩), Chuan-Kui Wang(王传奎), Zong-Liang Li(李宗良), and Shuai Qiu(邱帅)
Chin. Phys. B, 2024, 33 (**4**): 047201. DOI: 10.1088/1674-1056/ad1e65

Valley filtering and valley-polarized collective modes in bulk graphene monolayers

Jian-Long Zheng(郑建龙) and Feng Zhai(翟峰)
Chin. Phys. B, 2024, 33 (**1**): 017203. DOI: 10.1088/1674-1056/acfd17

Doping tuned anomalous Hall effect in the van der Waals magnetic topological phases $Mn(Sb_{1-x}Bi_x)_4Te_7$

Xin Zhang(张鑫), Zhicheng Jiang(江志诚), Jian Yuan(袁健), Xiaofei Hou(侯骁飞), Xia Wang(王霞),Na Yu(余娜), Zhiqiang Zou(邹志强), Zhengtai Liu(刘正太), Wei Xia(夏威),Zhenhai Yu(于振海), Dawei Shen(沈大伟), and Yanfeng Guo(郭艳峰)
Chin. Phys. B, 2023, 32 (**9**): 097201. DOI: 10.1088/1674-1056/acd629

Controlled crossover of electron transport in graphene nanoconstriction: From Coulomb blockade to electron interference

Wei Yu(余炜), Xiao Guo(郭潇), Yuwen Cai(蔡煜文), Xiaotian Yu(俞晓天), and Wenjie Liang(梁文杰)
Chin. Phys. B, 2023, 32 (**7**): 077202. DOI: 10.1088/1674-1056/accf67

High-performance spin-filtering and spin-rectifying effects in Blatter radical-based molecular spintronic device

Chun-Xu Tong(童春旭), Peng Zhao(赵朋), and Gang Chen(陈刚)
Chin. Phys. B, 2023, 32 (**6**): 067202. DOI: 10.1088/1674-1056/acc16d

---

Electronic transport evolution across the successive structural transitions in $Ni_{50-x}Fe_xTi_{50}$ shape memory alloys

Ping He(何萍)[1,2], Jinying Yang(杨金颖)[1,2], Qiusa Ren(任秋飒)[1,3], Binbin Wang(王彬彬)[1], Guangheng Wu(吴光恒)[1], and Enke Liu(刘恩克)[1,†]

[1] *Beijing National Laboratory for Condensed Matter Physics, Institute of Physics, Chinese Academy of Sciences, Beijing* 100190, *China*
[2] *School of Physical Sciences, University of Chinese Academy of Sciences, Beijing* 100049, *China*
[3] *School of Materials Science and Engineering, University of Science and Technology of Beijing, Beijing* 100083, *China*

(Received 14 February 2024; revised manuscript received 20 March 2024; accepted manuscript online 3 April 2024)

TiNi-based shape memory alloys have been extensively investigated due to their significant applications, but a comprehensive understanding of the evolution of electronic structure and electrical transport in a system with martensitic transformations (MT) is still lacking. In this work, we focused on the electronic transport behavior of three phases in $Ni_{50-x}Fe_xTi_{50}$ across the MT. A phase diagram of $Ni_{50-x}Fe_xTi_{50}$ was established based on x-ray diffraction, calorimetric, magnetic, and electrical measurements. To reveal the driving force of MT, phonon softening was revealed using first-principles calculations. Notably, the transverse and longitudinal transport behavior changed significantly across the phase transition, which can be attributed to the reconstruction of electronic structures. This work promotes the understanding of phase transitions and demonstrates the sensitivity of electron transport to phase transition.

Keywords: martensitic transformation, electronic behavior, transport properties, first-principles calculations

PACS: 72.15.–v **DOI:** 10.1088/1674-1056/ad39d3

1. Introduction

TiNi-based alloys are extensively utilized across various fields, including industry, military technology, and health care.[1–3] These alloys are primarily renowned for their exceptional superelasticity[4] and shape memory effects.[5] In the simplest instance of such materials, the shape memory effect in a binary NiTi alloy system is driven by martensitic transformation (MT).[2] MT is diffusionless transformation of a crystal structure, characterized by the coordinated movement of atoms, which results in the parent phase and the emerging new phase sharing the same composition and atomic sequence.[6–8] However, even for such a straightforward binary system material, numerous crucial questions remain unclear, including the evolution of electronic structure and transport properties across the MT.

The tuning of the martensitic transition temperature (T_{MT}) is of paramount importance in numerous applications involving shape memory alloys as it significantly influences the functionality and performance of these materials at working temperature. It has been observed that the composition of TiNi-based alloy exerts a substantial influence on the T_{MT}, as corroborated by both experimental and theoretical studies.[9–11] Additionally, the presence of precipitation within the system also affects the T_{MT}.[12] It has been proposed that the structural transformation can be induced by the band Jahn–Teller effect. Due to the presence of a high density of states at the Fermi level, the system becomes unstable and undergoes transformation to a more stable state via partial splitting and shifting of a band.[12,13] There are also some reports indicating that phonons play a crucial role in the NiTi phase transition mechanism.[14–16] It is the presence of soft modes that triggers the MT. Soft modes result from the coupling of phonons with Fermi surface-related electronic states and are the source of phonon anomalies and soft phonons in NiTi.[17,18] In previous studies, the most investigated aspects of NiTi-based systems have been their mechanical properties,[19] stability,[20] and the alteration of their microstructure due to heat treatment.[21] MT is characterized by abrupt changes in crystal structure, accompanied by profound alterations in electron structure and electron transport behavior.[4,5] The transport behavior and electronic structure across the MT remains scarcely reported. We expect to comprehend the electronic transport behavior across the MT in $Ni_{50-x}Fe_xTi_{50}$ alloys by using transverse and longitudinal measurements to provide further insight into the MT phenomenon.

Within this work, we introduce the Fe element to fine-tune the T_{MT}. A systematic investigation of the transformation behavior of $Ni_{50-x}Fe_xTi_{50}$ with varying Fe content is presented. By combining experiments and first principles calculations, the stability of the phase and the interplay between the electron structure and electron transport behavior across the MT are investigated.

2. Experiment and calculations

A series of polycrystalline $Ni_{50-x}Fe_xTi_{50}$ ($x = 0$, 2, 4, 6, 7, 8) alloys were prepared by repeated arc melting of appropriate quantities of constituent elements, namely, 99.995% Ni, 99.995% Ti, and 99.95% Fe in an argon atmosphere. The al-

†Corresponding author. E-mail: ekliu@iphy.ac.cn

© 2024 Chinese Physical Society and IOP Publishing Ltd

loys underwent four melting cycles to ensure a homogeneous composition. All the ingots were sealed in evacuated quartz tubes and kept at 1273 K for 3 days. Then, the samples were quenched into iced water. The samples were then cut into suitable shapes for different experiments.

X-ray diffraction (XRD) experiments were conducted using a SmartLab instrument with a compact ultra-low temperature chiller to detect any potential structural alterations associated with temperature changes. To reveal any possible phase transitions in our samples as a function of temperature, a simultaneous differential scanning calorimeter (DSC) device was used. The DSC experiments were carried out on a DSC 214 with a cooling and heating rate of 10 K/min. Magnetic properties were investigated using a superconducting quantum interference device (MPMS, Quantum Design) magnetometer. The transport properties were measured using the DC resistivity option of the physical property measurement system (PPMS, Quantum Design).

First-principles calculations based on density-functional theory (DFT)[22] were performed using the projector-augmented wave (PAW) method as implemented in the Vienna *ab initio* simulation (VASP) package.[23] The local-density approximation (LDA) functional was used as the exchange–correlation functional. The cut-off energy of the plane wave basis was set to 550 eV for the B2 structure and 600 eV for the R and B19′ phases. All the structures were fully relaxed until the force on each atom was smaller than 0.001 eV/Å. The first Brillouin zone of the reciprocal space was sampled with Monkhorst–Pack k-point meshes of $51\times51\times51$ and $18\times12\times11$ for the B2 and B19′ phases, and G-point meshes of $18\times18\times19$ for the R phase in self-consistency calculation. The tetrahedron method was used to calculate the density of states (DOS). The Phonopy package[24] was used to obtain phonon dispersion, and the harmonic force constants were calculated in $4\times3\times3$, $2\times2\times2$ and $4\times4\times4$ supercells for the B19′, R and B2 phases, respectively.

3. Results and discussion

3.1. Characterization of composition, structure and thermal analysis

The alloy numbers corresponding to each composition will be adopted in the subsequent sections of this work. The XRD spectra of $Ni_{50-x}Fe_xTi_{50}$ alloys with $x = 0$, 2, 4, 6, enlarged in the range of $40^\circ \leq 2\theta \leq 46^\circ$ and the DSC results are depicted in Figs. 1(a)–1(d) and 2(a), respectively. It can be seen that when the Fe content in $Ni_{50-x}Fe_xTi_{50}$ is relatively low ($x = 0$, 2, 4), the distinct exothermic and endothermic peaks observed on the cooling and heating DSC curves correspond to forward and reverse MTs,[25] respectively, which is consistent with the characteristics of the first-order transitions.[26] The schematic structures of B2 (cubic $Pm\bar{3}m$), R (rhombohedral $P3$), and B19′ (monoclinic $P2_1/m$) are shown in Figs. 1(e)–1(g). An analysis of the XRD results indicates that the Fe0 sample undergoes B2–B19′ one-step MT during cooling from 415 K to 300 K, as evidenced by the splitting of a single peak, which corresponds to only one peak of the DSC curve during the cooling process. Similarly, the XRD spectra of Fe4 samples exhibits the splitting of a single peak corresponding to the B2 structure at high temperature as the temperature decreases from 300 K to 200 K. In contrast to the Fe0 sample, the Fe4 sample exhibits an R structure at low temperature, suggesting a B2–R one-step MT. Fe_2 sample undergoes B2–R–B19′ MT during the temperature decrease from 350 K to 100 K, which corresponds to two peaks of the DSC curve during the cooling process. However, no MT (the B2 peak remains unchanged) is observed in the XRD spectra within the considered temperature range (from 250 K to 150 K) when the Fe content was increased to Fe6 in $Ni_{50-x}Fe_xTi_{50}$. It can be discerned that the width of the peak corresponding to the B2 structure has increased abnormally, revealing subtle microstructural changes, even in regions without MT.[27] The presence of minor peaks (represented by *) at both 250 K and 150 K are background (Cu) peaks, as observed in Fig. 1(d). Moreover, it is evident that an increase in Fe content leads to a shift of the endothermic and exothermic peaks towards lower temperatures and weakening of the peak intensity in the DSC curves, which indicates that the T_{MT} dramatically decreases and the enthalpy change gradually declines with the increase in the doping amount. Similarly, Fe doping in Heusler alloy $(Ni_{45.3}Fe_{5.3})$ $Mn_{23.8}Ga_{25.6}$ stabilized the austenitic phase down to 10 K with the vanishing of MT due to the addition of Fe.[28] In $Ni_{50-x}Fe_xMn_{40}Sn_{10}$ ($x = 0$, 2, 4, 6, 8 at.%) melt-spun ribbons, the T_{MT} decreases with the increase in Fe doping.[29]

Table 1. The alloy numbers and nominal compositions for the six alloy compositions.

Alloy number	Nominal compositions
Fe0	$Ni_{50}Ti_{50}$
Fe2	$Ni_{48}Fe_2Ti_{50}$
Fe4	$Ni_{46}Fe_4Ti_{50}$
Fe6	$Ni_{44}Fe_6Ti_{50}$
Fe7	$Ni_{43}Fe_7Ti_{50}$
Fe8	$Ni_{42}Fe_8Ti_{50}$

A simple phase diagram of the $Ni_{50-x}Fe_xTi_{50}$ system was obtained using XRD, DSC, magnetic and electrical transport measurements. The characteristic temperatures obtained from the DSC curves are summarized in Fig. 2(b). The results show that the characteristic temperatures obtained from the DSC, M–T, and ρ_{xx}–T curves are highly consistent with each other. The T_{MT}, namely, M_R: B2–R MT starting temperature, and $M_{B19'}$: R–B19′ MT starting temperature, were defined using the intersection of the base line and the tangent line with the largest slope of the peak. The T_{nd} at which the electrical resistivity begins to deviate from linearity is the start of

the ergodicity-breaking temperature.[27] To summarize, the results reveal the strong dependence of the T_{MT} on the Fe content, with an observed decrease in the T_{MT} as the Fe content increases in $Ni_{50-x}Ti_{50}Fe_x$. Moreover, there is a critical point where a normal MT transitions into abnormal non-transforming behavior. This phenomenon has also been reported in the literature.[30] Interestingly, a two-step MT occurs when an appropriate amount of Fe is introduced as dopant. In the Fe2 sample, distinct phases emerge within different temperature ranges, providing a suitable material system for investigating the intricate relationship between electrical transport behavior and electronic structure evolution across the MT.

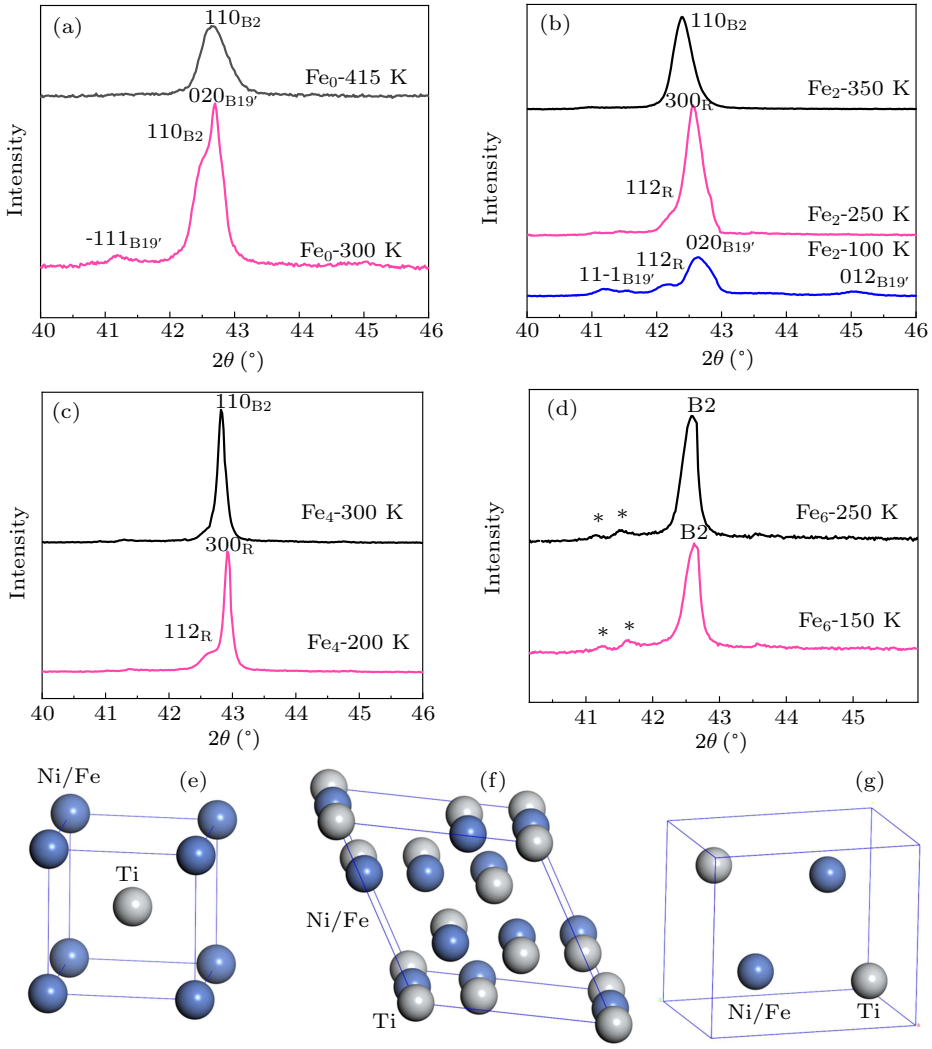


Fig. 1. XRD spectra of $Ni_{50}Ti_{50}$ (a), $Ni_{48}Fe_2Ti_{50}$ (b), $Ni_{46}Fe_4Ti_{50}$ (c), and $Ni_{44}Fe_6Ti_{50}$ (d) at different temperatures. The structure of $Ni_{50}Ti_{50}$: (e) B2 phase, (f) R phase, and (g) B19′ phase.

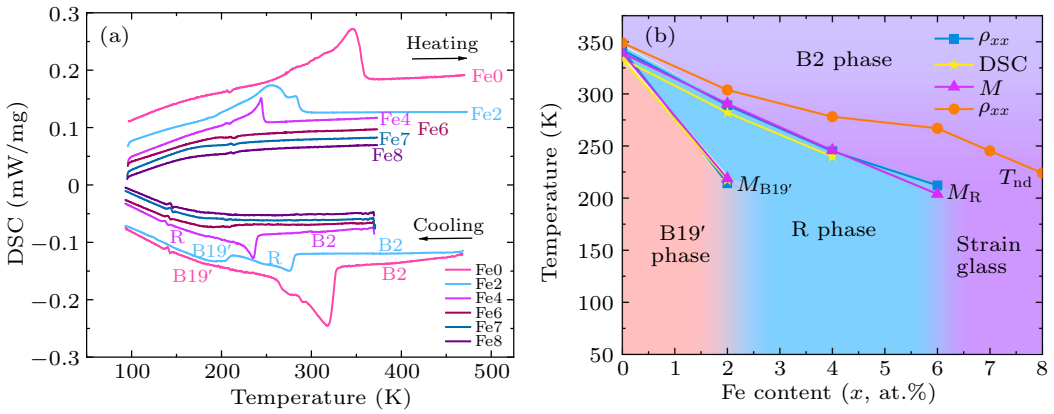


Fig. 2. (a) DSC curves of $Ni_{50-x}Fe_xTi_{50}$ alloys with different Fe content ($x = 0$, 2, 4, 6, 7, 8). (b) A phase diagram of the $Ni_{50+x}Ti_{50-x}Fe_x$ system. The yellow, blue, and purple points, respectively, show the phase transformation temperatures from the DSC, electric resistivity, and magnetization measurements. The orange points are T_{nd}, which is the start of the ergodicity-breaking temperature through fitting the electrical resistivity results. Here, M_R and $M_{B19'}$ are the normal R phase and B19′ phase T_{MT}.

3.2. Phonon-dispersion spectra and density of states

To better understand the driving force of MT in $Ni_{50-x}Fe_xTi_{50}$ and the change in physical properties caused by martensitic structural transformation, first principles calculations were employed to calculate the phonon dispersions of the three phases (B2, R and B19′). In the $Ni_{50-x}Fe_xTi_{50}$ alloy system, Fe atoms chemically replace Ni atoms and directly take the sites of Ni atoms. This substitution is attributed to the formation of d–d hybridization bonding between Ni/Fe atoms and Ti atoms.[31,32] Due to the difficulty of first-principles calculations for compositions with low-level doping, the stoichiometric $Ni_{50}Ti_{50}$ was chosen for calculations. The structures are shown in Figs. 1(e)–1(g). The phonon dispersions of the B2, R, and B19′ phases along high symmetry paths, calculated in the ground state, are presented in Figs. 3(a)–3(c), respectively. The presence of imaginary phonon modes manifests that the crystal structure is dynamically unstable, indicating the formation of a new structure with reduced energy.[33,34] As expected, based on the experimental observations, the B2 and R structures exhibit instability at low temperatures, whereas the B19′ structure remains stable. For the B2 structure, at the Γ point, the acoustic branches behave normally at very small q. As q increases along the Γ–R and Γ–M, the acoustic branches disperse, experience a drastic decline, and then become dynamically unstable. For the R structure, the presence of imaginary modes centered on the Γ point indicates structural instability. Conversely, for the B19′ structure, the phonon dispersions remain positive over the entire Brillouin zone, indicating inherent structural stability. The presence of virtual frequencies in the calculated phonon dispersions depicted in Figs. 3(a)–3(c) signifies the occurrence of phonon softening within the system. Phonon interaction results in different alterations to phonon frequencies across different modes, thus lifting the phonon degeneracy and leading to phonon energy-level splitting.[35] Consequently, this leads to a reduction in total phonon energy, enhancing structural stability.

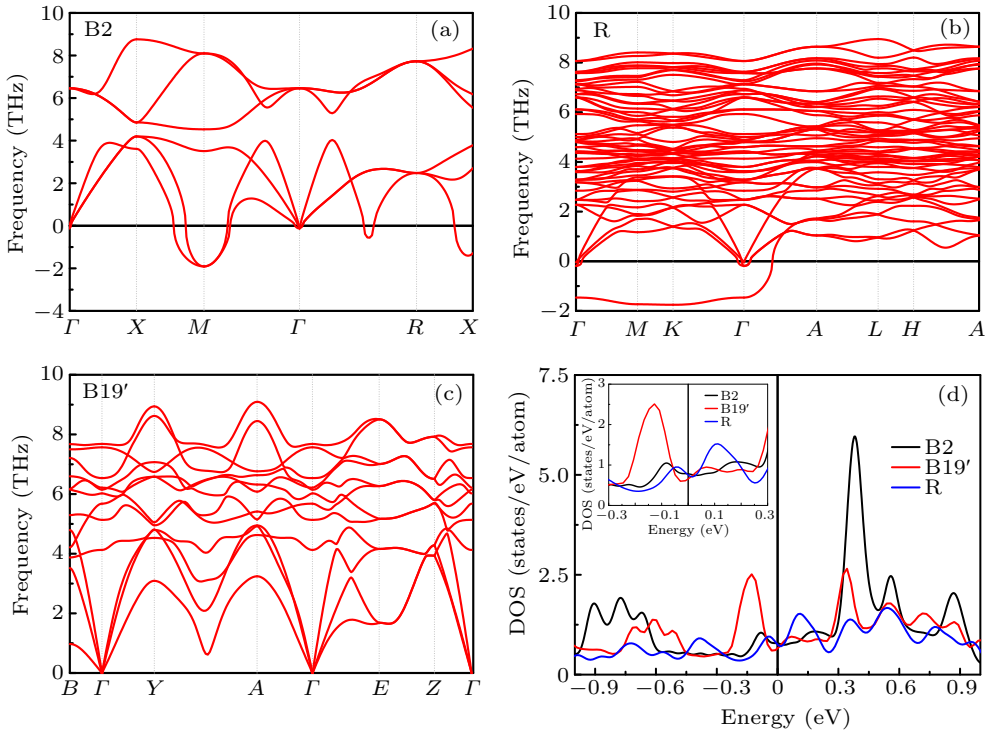


Fig. 3. Calculated phonon-dispersion spectra of NiTi for (a) B2, (b) R and (c) B19′ structures. (d) Calculated DOS near the Fermi level of NiTi. The inset shows a magnification of the DOS near the Fermi level.

To further investigate the electronic properties of $Ni_{50-x}Fe_xTi_{50}$, the DOS of the B2, R, and B19′ at the Fermi level were calculated using first-principles calculations. As shown in Fig. 3(d), all the phases exhibit metallic behavior, with the valence band and conduction band overlapping, while exhibiting a significantly high DOS at the Fermi level. MT is commonly understood as electronic structure instability, according to the band Jahn–Teller effect,[36–38] which induces band reconstruction and lattice distortion due to a high density of states near the Fermi level. Conversely, reducing the density of states near the Fermi level enhances the structural stability. Our calculations and experiments support this theory, as the B2 structure exhibits the highest density of states near the Fermi level and undergoes an MT, while the R structure represents an intermediate phase with an unstable structure. Finally, the B19′ structure has the lowest density of states near the Fermi level, and thus displays the most stable structure. The DOS calculation results align with the obtained results from dispersion spectra. By considering the change trend of the calculated electronic structures for the three phases (B2, R and B19′) and the experimental decrease in T_{MT} with the increase in Fe doping, one can deduce that the addition of Fe can

lower the high density of states at the Fermi level of the parent phase, in order to eliminate the instability of the parent phase. The DOS (Fig. 3(d)) of the three phases are completely different, which indicates that the band structure is largely different and that transport behavior will thus be different. This is the main reason why electronic transport can be used for studying the phase transition.

3.3. Magnetization

The temperature dependence of the magnetization curves (M–T) of all the alloys at 1 kOe are illustrated in Fig. 4(a). The characteristic temperature obtained from the M–T curves are also summarized in Fig. 2(b). In the M–T cooling curve of the Fe0 alloy, a pronounced decline in the M–T curve signifies the occurrence of B2–B19′ MT. The results demonstrate rectangular thermal hysteresis of magnetization, with both the austenite and martensite exhibiting temperature-dependent magnetization characteristics. In the M–T cooling curve of the Fe2 alloy, the magnetization exhibits a pronounced decrease at temperatures of 290 K and 219 K, indicating a two-step transition in this sample. These MTs correspond to the B2–R and the subsequent R–B19′ phase transitions. Notably, the B2–R phase transitions are characterized by narrow hysteresis (weak first-order) behavior, while the R–B19′ phase transition displays wide hysteresis (strong first-order) characteristics. Upon cooling of the Fe4 and Fe6 samples, the magnetization curves show a pronounced decrease at 246 K and 204 K, respectively. In the Fe6 sample, no evidence of MT was detected by XRD and DSC. However, notable thermal hysteresis, which originates from the nucleation barrier[39] that needs to be overcome in the early stage of the transformation, was observed in the M–T curves, indicating the occurrence of MT. The magnetization is notably responsive to structural alterations, enabling it to detect the elusive signal. Upon cooling of the Fe7 and Fe8 samples, although there are some noticeable increases in magnetization, no discernible thermal hysteresis is observed, suggesting the absence of an apparent MT. In addition, as the doping amount of Fe in $Ni_{50-x}Fe_xTi_{50}$ increases, the magnetization exhibits a corresponding rise, potentially attributed to the larger magnetic moment of Fe compared to Ni.[30] At the same time, the findings reveal that as the temperature decreases, the sample undergoes MT, leading to a decline in its magnetization. The symmetry of the crystal decreases (B2: cubic, R: trigonal, B19′: monoclinic) and the magnetocrystalline anisotropy increases across the MT,[40] resulting in a decrease in magnetization at low fields. It has also been found that the magnetization and symmetry decrease sharply in a $Ni_{44}Mn_{45-x}Fe_xSn_{11}$ ($x = 0, 1, 2$) system across MT.[41] However, it has been found that the magnetization increases and the symmetry decreases during the martensitic phase transition in $Fe_{45}Mn_{26}Ga_{29}$ alloy.[42]

The magnetization behavior under varying magnetic fields is presented in Fig. 4(b), where the respective measuring temperatures are designated by arrows in Fig. 4(a). It is evident that the samples exhibit predominantly paramagnetism in the B2, R and B19′ phases. The initial magnetization of martensite is relatively low due to the increased magnetocrystalline anisotropy compared with the parent phase, as depicted in the inset of Fig. 4(b). However, all the phases demonstrate weak ferromagnetism only in very low magnetic fields, which may be attributed to defects in the samples.[43]

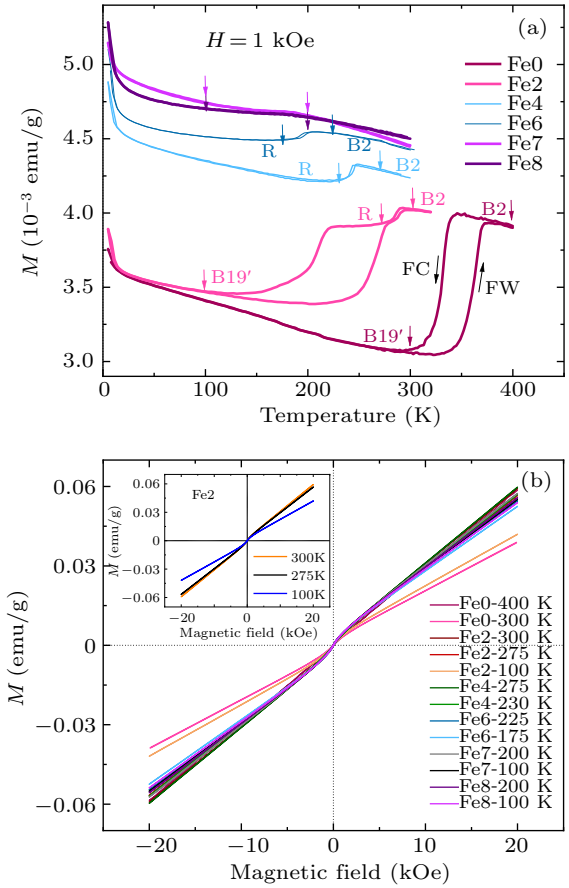


Fig. 4. (a) The M–T curves of $Ni_{50-x}Fe_xTi_{50}$ ($x = 0$, 2, 4, 6, 7, 8) at 1 kOe, showing MTs from the B2 parent phase to different martensite phases. (b) Magnetization curves up to 20 kOe. The measuring temperature is depicted in Fig. 3 (a) via color-coded arrows (the arrow colors correspond to the curve colors).

3.4. Electrical resistivity and Hall measurements

The temperature dependence of the longitudinal resistivity curves (ρ_{xx}–T) at zero magnetic field is illustrated in Fig. 5(a). The characteristic temperatures obtained from the ρ_{xx}–T curves are summarized in Fig. 2(b). The ρ_{xx} initially exhibits a significant increase on the ρ_{xx}–T curve, followed by a sharp peak and subsequent decline during the cooling process of the Fe0 sample. This peak corresponds to the B2–B19′ transition and different $d\rho_{xx}/dT$ observed in the low and high temperature regions indicates the different phases. The origin of this transport anomaly may be attributed to the presence of a phase boundary between B2 and B19′. The phase boundary introduces additional scattering events, leading to an increase in resistivity across the MT.[44] After the completion of the MT, this phase boundary disappears, resulting in a drop in resistiv-

ity. Upon cooling of the Fe2 sample, ρ_{xx} exhibits a pronounced increase at 289 K and a sharp decrease at 214 K, corresponding to the T_{MT} of the B2–R and R–B19′ phases, respectively. Upon cooling of the Fe4 and Fe6 samples, ρ_{xx} manifests a pronounced increase at 245 K and 212 K, respectively, corresponding to the T_{MT} of B2–R MT. The MT can also be observed in the Fe6 sample by using the resistivity measurement, which cannot be observed in the DSC measurement. The Fe7 and Fe8 samples do not exhibit MT over the measured temperature range due to the vanishing of the thermodynamic force, which is consistent with the M–T curves.

The carrier concentration can more intuitively show the change in the band structure near the Fermi level caused by structural change. To acquire a more profound comprehension of the transport properties exhibited by this system, the transverse Hall resistivity of the Fe2 sample was measured. The measured results are presented in Fig. 5(b). A linear dependence of ρ_{yx} indicates the ordinary Hall effect with positive slopes for all the phases (B2, R, B19′). The positive Hall coefficient suggests that the primary carriers in the sample are holes. The $\rho_{xy} = -B/(ne)$ and $\mu = 1/(ne\rho_{xy}(B = 0))$ equations were employed to calculate the charge carrier concentration and carrier mobility. Figures 5(c) and 5(d) show that in the B2 and R phases, n decreases while μ experiences a slight increase with decreasing temperature. In the B19′ phases, n declines and the mobility increases as the temperature decreases. There are sudden changes in n, which exhibits the sensitivity of transverse transport to structure changes across the B2–R and R–B19′ MTs.

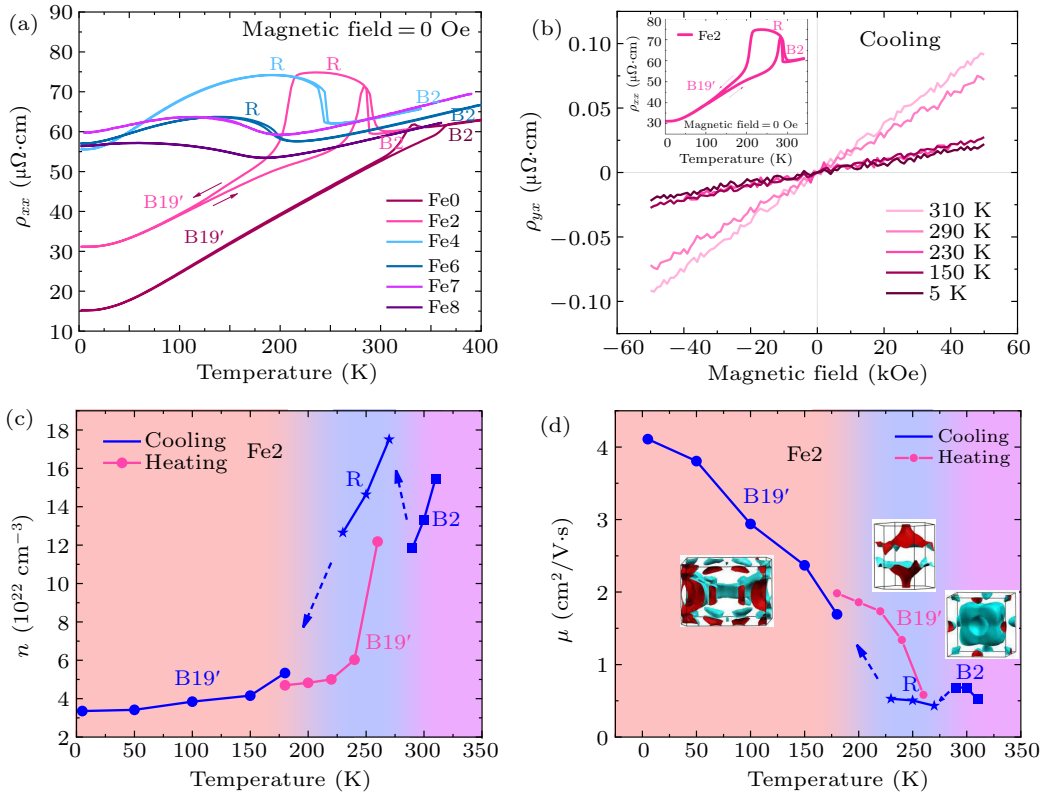


Fig. 5. (a) The ρ_{xx}–T curves of $Ni_{50-x}Fe_xTi_{50}$ ($x = 0, 2, 4, 6, 7, 8$) in the zero field. (b) The magnetic field dependence of Hall resistivity ρ_{xy} at various temperatures of Fe2. The temperature dependence of (c) the carrier concentration (n) and (d) mobility (μ) of Fe2. In (b) and (c), the sample in phase B2 is represented by the boxes, while the sample in phase R is denoted by pentagram stars, and the sample in phase B19′ is symbolized by the circles. The green curve depicts the measurements obtained during cooling, while the fluorescent green curve illustrates the measurements acquired during warming.

In the Fe2 sample, the holes serve as the primary carrier and dominate the transport properties. The carrier concentration exhibits significant changes across the MT, with a 48% increase observed across the B2–R phase transition and an order of magnitude decrease across the R–B19′ MT. The n is an intrinsic parameter, which is determined by the band structure around the Fermi level.[45] The sudden change in n can be further understood from the view of the Fermi surface and DOS. As depicted in the inset of Fig. 5(d), the Fermi surface of B2 exhibits a cubic-like shape, characterized by a smooth and flat nature. The Fermi surface of the R phase adopts a configuration resembling two umbrella shapes and becomes more anisotropic across the B2–R phase transition. Subsequently, there is a transformation in which the Fermi surface shape of B19′ becomes thinner and fragmented but well distributed across the R–B19′ phase transition, corresponding to a high conductivity and low resistivity. The varying DOS around the Fermi level and the different Fermi surfaces of the three phases are consistent with the change in n across the MT (Figs. 3(d) and 5(d)). Sudden changes in the n can be used to reveal

changes in the crystal structure across the MT. Similarly, in the $Ni_{50-x}Fe_xMn_{35}Ti_{15}$ system, the T_{MT} decreases with the increase in the Fe content, and the calculation results also show that the total DOS around the Fermi level decreases with the increase in Fe content. When the system changed from the B2 phase to 5M and $L1_0$ martensite phases, the high DOS value is reduced by electronic redistribution and a reduction in instability is achieved. A sharp change in the hole carrier concentration was observed across the MT.[36]

From the expression of mobility ($\mu = q\tau/m^*$, τ is the relaxation time and m^* is the effective mass of carriers), it can be seen that the mobility is determined by the intrinsic energy bands and the extrinsic scattering. Different crystal structures correspond to different electronic band structures and different m^*. The τ is usually determined by a variety of scattering, including phonon–phonon scattering and impurity scattering.[46] The sudden change in μ across the MT can also be observed in our experimental results (Fig. 5(d)), which may be related to the change in the band structure around the Fermi level and electronic–phonon scattering. According to the relation of $\rho_{xx} = 1/(nq\mu)$, the sudden change in n and μ leads to the sudden change in electronic resistivity across the MT (Fig. 5(a)). Similarly, the carrier mobility of the $Ni_{50-x}Fe_xMn_{35}Ti_{15}$ system is depressed due to the lattice distortion and the altered topology of the Fermi surface. The variation in transport properties stems from the reconstruction of the electronic structure during the MTs.[36] Transport can directly reflect the information of the crystal structure and the band structure via the change in the carrier concentration, and it is easy to obtain, which makes electric transport a good method for the study of phase transformation.

4. Summary

A temperature–composition phase diagram is established using structural analysis, thermal analysis, magnetic and transport properties. The martensitic transition temperature in the Fe-doped ternary $Ni_{50-x}Fe_xTi_{50}$ alloy gradually decreases with increasing Fe content, and the martensitic transition is suppressed when $x > 6$. Based on experiments and first-principles calculations, it is demonstrated that phonon softening leads to instability of the structure and martensitic transition. The transport properties show that the abrupt changes in carrier concentration across the martensitic transition are consistent with the change in the DOS and Fermi surface. The modification in transport properties stems from the reconstruction of the electronic structure across the phase transition, providing significant evidence for elucidating the correlation between electronic transport properties and phase transition.

Acknowledgements

This work was supported by the State Key Development Program for Basic Research of China (Grant Nos. 2019YFA0704900 and 2022YFA1403800), the Fundamental Science Center of the National Natural Science Foundation of China (Grant No. 52088101), the Strategic Priority Research Program (B) of the Chinese Academy of Sciences (CAS) (Grant No. XDB33000000), the Synergetic Extreme Condition User Facility (SECUF), and the Scientific Instrument Developing Project of CAS (Grant No. ZDKYYQ20210003).

References

[1] Otsuka K and Kakeshita T 2002 *MRS Bull.* **27** 91
[2] Shaw J A and Kyriakides S 1995 *J. Mech. Phys. Solids* **43** 1243
[3] Lobo P S, Almeida J and Guerreiro L 2015 *Proc. Eng.* **114** 776
[4] Yamauchi K, Ohkata I, Tsuchiya K and Miyazaki S 2011 *Shape memory and superelastic alloys* (Cambridge: Woodhead Publishing) pp. 163–168
[5] Huang W M, Ding Z, Wang C C, Wei J, Zhao Y and Purnawali H 2010 *Mater Today* **13** 54
[6] Tegus O, Brück E, Buschow K H and de Boer F R 2002 *Nature* **415** 150
[7] Giot M, Chapon L C, Androulakis J, Green M A, Radaelli P G and Lappas A 2007 *Phys. Rev. Lett.* **99** 247211
[8] Yu M H, Lewis L H and Moodenbaugh A R 2003 *J. Appl. Phys.* **93** 10128
[9] Sarkar S, Ren X and Otsuka K 2005 *Phys. Rev. Lett.* **95** 205702
[10] Zhang J, Somsen C, Simon T, Ding X, Hou S, Ren S, Ren X, Eggeler G, Otsuka K and Sun J 2012 *Acta Mater.* **60** 1999
[11] Hu L, Jiang S, Liu S, Zhang Y, Zhao Y and Zhao C 2016 *Mater. Sci. Eng. A* **660** 1
[12] Schryvers D, Tirry W and Yang Z 2004 *MRS Online Proceedings Library* **842** 156
[13] Allafi J K, Dlouhy A and Eggeler G 2002 *Acta Mater.* **50** 4255
[14] Wu Z and Lawson J W 2022 *Phys. Rev. B* **106** L140102
[15] Haskins J B, Thompson A E and Lawson J W 2016 *Phys. Rev. B* **94** 214110
[16] Haskins J B and Lawson J W 2017 *J. Appl. Phys.* **121** 205103
[17] Satija S K, Shapiro S M, Salamon M B and Wayman S M 1984 *Phys. Rev. B* **29** 6031
[18] Moine P, Allain J and Renker B 1984 *J. Phys. F: Met. Phys.* **14** 2517
[19] Swain B, Mallick P, Bhuyan S K, Mohapatra S S, Mishra S C and Behera A 2020 *J. Therm. Spray. Tech.* **29** 741
[20] Kaya M, Çakmak Ö, Gülenç B and AtlıK C 2017 *Mater. Res. Bull.* **95** 243
[21] Zhu J N, Zhu W, Borisov E, Yao X, Riemslag T, Goulas C, Popovich A, Yan Z, Tichelaar F D, Mainali D P, Hermans M and Popovich V 2023 *J. Alloys Compd.* **967** 171740
[22] Kohn W and Sham L J 1965 *Phys. Rev.* **140** A1133
[23] Kresse G and Furthmüller 1996 *Phys. Rev. B* **54** 11169
[24] Togo A, Oba F and Tanaka L 2008 *Phys. Rev. B* **78** 134106
[25] Lohan N M, Pricop B, Burlacu L and Bujoreanu L G 2018 *J. Therm. Anal. Calorim.* **131** 215
[26] Liu J, Wang L, Niu M, Jiang R, Liu Y J, Xu D and Jin C G 2021 *J. Magn. Magn. Mater.* **527** 167777
[27] Wang D, Zhang Z, Zhang J, Zhou Y, Wang Y, Ding X, Wang Y and Ren X 2010 *Acta Mater.* **58** 6206
[28] Kopecký V, Rameš M, Veřtát P, Colman R H and Heczko O 2021 *Metals* **11** 850
[29] Aguilar-Ortiz C O, Soto-Parra D, Alvarez-Alonso P, Lazpita P, Salazar D, Castillo-Villa P O, Flores-Zúnig H and Chernenko V A 2016 *Acta Mater.* **107** 9
[30] Lázpita P, Sasmaz M, Barandiarán J M and Chernenko V A 2018 *Acta Mater.* **155** 95

[31] Agrawal A, Bakhtiari S, Mirzaeifar R, Jiang D, Yang H and Liu Y N 2024 *J. Alloys Compd.* **976** 172969
[32] Parida J, Mishra S C, Satapathy D K, Marupalli B C G and Behera A 2023 *J. Materi Eng. Perform.*
[33] Nepal N K, Canfield P C and Wang L L 2024 *Phys. Rev. B* **109** 054518
[34] Malcherek T and Fischer M 2018 *Phys. Rev. Mater.* **2** 023602
[35] Jin Y M, Wang Y U and Ren Y 2015 *npj Comput. Mater.* **1** 15002
[36] Zeng Q Q, Shen J L, Zhang H N, Chen J, Ding B, Xi X K, Liu E K, Wang W H and Wu G H 2019 *J. Phys.: Condens. Matter* **31** 425401
[37] Lin T T, Dai X F, Zhao J X, Wang L Y, Wang X T, Cui Y T and Liu G D 2016 *J. Alloys Compd.* **684** 143
[38] Algethami O A, Zhang Q Q, Tan J G, Wang X T, Liu Z H and Ma X G 2020 *J. Magn. Magn. Mater.* **498** 166252
[39] He B B and Shang X K 2021 *Philos Mag. Lett.* **101** 417
[40] Fukuda T, Maeda H, Yasui M and Kakeshita T 2008 *Scripta Mater.* **60** 261
[41] Ouyang J, Tian Y, Xiao H and Zhang Y 2021 *Mater. Chem. Phys.* **273** 125150
[42] Kudryavtsev Y V, Uvarov N V, Perekos A E, Dubowik J and Kozlova L E 2019 *Intermetallics* **109** 85
[43] Malik S V, Dias E T, Babu P D and Priolkar K R 2023 *J.Phys.: Condens. Matter* **36** 135701
[44] Kaletinaa Y V, Gerasimova E G, Terenteva P B and Kaletin A Y 2020 *Phys. Metals Metallogr.* **121** 894
[45] Kasap S, Koughia C, Ruda H and Johanson R 2007 *Springer Handbook of Electronic and Photonic Materials* (Boston, MA: Springer) pp. 20–23
[46] Kunzmann A, Frenzel J, Wolff U, Han J M, Giebeler L, Piorunek D, Mittendorff M, Scheiter J, Reith H, Perez N, Nielsch K, Eggeler G and Schierning G 2022 *Mater. Today Phys.* **24** 100671